PAPER • OPEN ACCESS

Ion-irradiation-assisted tuning of phase transformations and physical properties in single crystalline Fe_7Pd_3 ferromagnetic shape memory alloy thin films

To cite this article: A Arabi-Hashemi *et al* 2015 *New J. Phys.* **17** 053029

View the article online for updates and enhancements.

New Journal of Physics

The open access journal at the forefront of physics

CrossMark

PAPER

Ion-irradiation-assisted tuning of phase transformations and physical properties in single crystalline Fe_7Pd_3 ferromagnetic shape memory alloy thin films

A Arabi-Hashemi[1], R Witte[2], A Lotnyk[1], R A Brand[2], A Setzer[3], P Esquinazi[3], H Hahn[2], R S Averback[4] and S G Mayr[1,5]

[1] Leibniz-Institute for Surface Modification (IOM), Permoserstraße 15, 04318 Leipzig, Germany
[2] Institute of Nanotechnology, Karlsruhe Institute of Technology, Hermann-von-Helmholtz-Platz 1, 76344 Eggenstein-Leopoldshafen, Germany
[3] Division of Superconductivity and Magnetism, Faculty of Physics and Earth Sciences, University of Leipzig, 04103 Leipzig, Germany
[4] Department of Materials Science and Engineering, University of Illinois at Urbana-Champaign, Urbana, IL 61801, USA
[5] Translational Center for Regenerative Medicine and Faculty of Physics and Earth Sciences, University of Leipzig, 04103 Leipzig, Germany

E-mail: stefan.mayr@iom-leipzig.de

Keywords: martensitic transformations, ion irradiation, thermodynamics, shape memory materials, metallic alloys

Abstract

Control of multi-martensite phase transformations and physical properties constitute greatly unresolved challenges in Fe_7Pd_3-based ferromagnetic shape memory alloys. Single crystalline Fe_7Pd_3 thin films reveal an austenite to martensite phase transformation, continuously ranging from the face-centered cubic (fcc) to the face-centered tetragonal (fct) and body-centered cubic (bcc) phases upon irradiation with 1.8 MeV Kr^+ ions. Within the present contribution, we explore this scenario within a comprehensive experimental study: employing atomic force microscopy (AFM) and high resolution transmission electron microscopy (HR-TEM), we first clarify the crystallography of the ion-irradiation-induced austenite $\Rightarrow$ martensite and inter-martensite transitions, explore the multi-variant martensite structures with c-a twinning and unravel a very gradual transition between variants at twin boundaries. Accompanying magnetic properties, addressed locally and globally, are characterized by an increasing saturation magnetization from fcc to bcc, while coercivity and remanence are demonstrated to be governed by magnetocrystalline anisotropy and ion-irradiation-induced defect density, respectively. Based on reversibility of ion-irradiation-induced materials changes due to annealing treatment and a conversion electron Mößbauer spectroscopy (CEMS) study to address changes in order, a quantitative defect-based physical picture of ion-irradiation-induced austenite $\Leftrightarrow$ martensite transformation in Fe_7Pd_3 is developed. The presented concepts thus pave the way for ion-irradiation-assisted optimization strategies for tailored functional alloys.

1. Introduction

Since the discovery of the magnetic shape memory (MSM) effect in Ni-Mn-Ga with theoretical strains of up to 10% [1], MSM alloys have attracted increasing interest from both scientific and technological points of view. While the MSM effect in disordered Fe_7Pd_3 was reported in 1998 [2], the Fe–Pd alloy had been already extensively studied in the 1960s, primarily due to its invar properties [3, 4]. Later, ordered and tetragonal $L1_0$ FePd attracted interest for data storage applications due to its high uniaxial magnetocrystalline anisotropy [5]. Despite yielding lower maximum theoretical strains than Ni-Mn-Ga [6], Fe_7Pd_3 is characterized by attractive complementary materials properties, including an 'inverse' MSM effect when compared with Ni-Mn-Ga (Ni-Mn-Ga and Fe–Pd contract parallel and perpendicular to the direction of the magnetic field, respectively), much higher ductility and biocompatibility [7, 8], which paves the way for use in medical applications (e.g., as adjustable implants or active elements [9]). Fe_7Pd_3 exhibits four metastable phases at room temperature, viz. the austenite phase (fcc structure, γ-phase) and three martensite phases with fct, bct (body centered tetragonal), and

bcc lattices, each of which is characterized by a unique tetragonality, as described by the c/a ratio of the unit cell (1, 0.94, 0.72, and 0.707, respectively). Transitions between them can formally be described by the Bain transformation [10], while the complete fcc ⇔ bcc transition can be constructed by the combination of a Bain transformation, a rotation, and a lattice invariant shear (LIS), such as twinning or slip [11]; in the case of Fe_7Pd_3, twinning constitutes this LIS. However, as demonstrated recently [12], the Bain path formalism does not involve the correct description of the orientation relationship (OR) between the fcc and the bcc phase in Fe_7Pd_3, which follows an OR due to Nishiyama–Wassermann. Within this context it is worth emphasizing, that for the Fe_7Pd_3 system, both austenite and martensite are metastable around room temperature, while phase separation into α-iron (bcc) and Fe_5Pd_5 (L1$_0$ structure) constitutes thermal equilibrium. The MSM effect, on the other hand, is only observed in the martensite fct phase, since it fulfils the requirements of yielding sufficiently high magnetocrystalline anisotropy and twin boundary mobility [13]. Transformations to bct and bcc occur non-thermoelastically (that is, irreversibly), while the preconditions for the MSM effect are not fulfilled in these phases.

Starting from metastable phase diagrams for the austenite and martensite phases in Fe–Pd, it has been established that compositional changes as low as 0.1 at% severely affect the austenite ⇔ martensite transition temperature [14–17]. Additional shifts in favor of martensite have been established to arise by presence of shear stresses, as described by the Clausius–Clapeyron equation [18]. They have also been suggested for modifications in the short-range order of the globally disordered phases based on computer calculations [19]. In fact, the basis for occurrence of these effects—in particular, the latter—is a very shallow energy landscape varying as little as ≈20 meV/atom along the Bain path [20, 21]. Due to an 'energetic proximity' among the phases as close as that, phase changes along the Bain path are in fact even in reach of so tiny changes in alloy topology, as short-range order. In fact, order disorder transformations have been demonstrated to severely impact the energy landscape, in particular the location of the energy minimum of the Bain transformation path of Fe_7Pd_3 and $Fe_{75}Pd_{25}$ ranging from fcc to bcc [19, 22]. While a fully disordered Fe_7Pd_3 system has its minimum ground state energy close to the bcc phase, a fully ordered system can minimize its ground state energy in the fcc structure. Thus, deviations from the equilibrium order configuration constitute an additional degree of freedom of the system that needs to be taken into account. Directly related to this, experimental synthesis of phase-pure fct Fe_7Pd_3, still poses challenges. While post-deposition annealing has been a method of choice [23], it has been demonstrated recently that deposition at elevated temperatures yields single crystalline Fe_7Pd_3 fct films directly [24]. Furthermore, lift-off approaches to obtain structurally, morphologically, and chemically intact freestanding MSM films have also been developed [25].

Recently we have reported about an x-ray diffraction (XRD) study indicating that ion irradiation allows for phase selection along the whole transformation path from fcc to bcc [12]. Based on the considerations outlined previously, irradiation of austenite Fe_7Pd_3 with energetic ions is expected to affect the phase in a twofold way, viz. by insertion of point defects and by modification of the short-range order within the globally disordered Fe_7Pd_3 alloy. The present study aims to systematically address the physical foundations underlying this behavior and report on comprehensive experimental characterization of ion-irradiation-induced modifications of physical properties in Fe_7Pd_3. In doing so, we first describe the phenomenology of the ion-irradiation-induced austenite ⇒ martensite transition employing high resolution imaging techniques in real space, viz. AFM, magnetic force microscopy (MFM), and HR-TEM, and address concurrently occurring modifications of global magnetic properties employing superconducting quantum interference device (SQUID) magnetometry. We then proceed by experimentally clarifying the physical mechanism that mediates phase transition by focusing on evolution of stress and short-range order in the course of ion irradiation treatment, employing CEMS measurements. Based on that, a comprehensive picture of the physics behind ion-irradiation-assisted phase selection in Fe_7Pd_3 will be developed, followed by a summary.

2. Experimental details

Fe_7Pd_3 films, 500 nm thick, were condensed onto single crystalline epi-polished MgO (001) by molecular beam epitaxy using two independently rate controlled electron beam evaporators in an ultra high vacuum (UHV) chamber (base pressure 3 10^{-9} mbar or better) [26, 27]. By using a total deposition rate of 0.15 nm s^{-1} at a substrate temperature of 1123 K, we were able to grow the films in their equilibrium gamma phase (austenite with a disordered fcc lattice) [28]. Subsequently they were rapidly quenched with aid of a liquid nitrogen shield to prevent decomposition into the stable room temperature phases, α-iron and L1$_0$ FePd. To verify the desired composition, the films were routinely analyzed by energy dispersive x-ray spectroscopy (EDX) using a Zeiss Ultra 55 field emission scanning electron microscope (SEM). In this study, five different Fe_7Pd_3 samples were presented, all of which had a geometry of 5 × 5 mm. Four of the five specimens were ion irradiated with 1.8 MeV Kr$^+$ ions under high vacuum conditions, while a fifth sample was left unirradiated. It should be emphasized at

Table 1. Summary of the different types of samples synthesized and investigated within the present study.

Sample#	Ion irradiation treatment (1.8 MeV Kr$^+$)	Displacements per atom (dpa) [31]	Composition (EDX)	Characterization (Section)
1	10^{14} ions cm^{-2}	0.1	71–29	CEMS (4.1)
2	5×10^{14} ions cm^{-2}	0.5		XRD (4.2)
3	5×10^{15} ions cm^{-2}	5		AFM, MFM, SQUID (3.3)
4	Unirradiated	0		HR-TEM (3.2)
5	10^{15} ions cm^{-2}	1	70–30	Post-annealing, XRD (3.4)

this point that the unirradiated and three irradiated specimens studied in section 3 were cut from one large 1×1 cm sample, thus guaranteeing completely identical preparation conditions. For one specific sample irradiated with 10^{15} ions cm^{-2} 1.8 MeV Kr$^+$ ions, an additional annealing treatment was performed to address reversibility of the austenite ⇒ martensite transformation by defect annihilation. Crystal structure, surface topography, and nanomagnetic properties were routinely characterized with XRD with a Seiffert XRD 3003 PTS using Cu Kα radiation and an Asylum MFP 3D AFM/MFM, employing Bruker micro etched silicon coated with chromium/cobalt probes. These had a coercivity of 400 Oe and a tip radius of 35 nm that were kept at a tip-sample distance of 40 nm during MFM measurements. To address microstructural changes, in particular with respect to the orientation of martensite domains (so-called 'variants') and the defect state after ion irradiation, HR-TEM, scanning transmission electron microscopy measurements (STEM), and selected area electron diffraction (SAED) were conducted on specific samples using a FEI Titan G2 60–300 microscope operating at 300 keV accelerating voltage. Global magnetic properties, including saturation magnetization, remanence, coercivity, and magnetic anisotropies were studied by a SQUID magnetometer MPMS-7 from Quantum Design with an external magnetic field aligned in-plane (parallel to MgO$_{[100]}$) and out-of-plane (parallel to MgO$_{[001]}$). CEMS was employed to track changes in short-range order. A ^{57}Co in Rh matrix source was used together with a constant acceleration drive. The conversion electrons were detected with a custom-built gas-proportional counter. The velocity scale was calibrated with a bcc Fe standard and all center (isomer) shifts are given relative to bcc Fe at room temperature. Stress levels within Fe$_7$Pd$_3$ austenite single crystal films atop of MgO single crystal substrates were obtained by the $\sin^2 \psi$ method [29, 30], employing various diffraction peaks. Table 1 summarizes all Fe$_7$Pd$_3$ samples presented within this work, their irradiation treatments, and resulting physical properties.

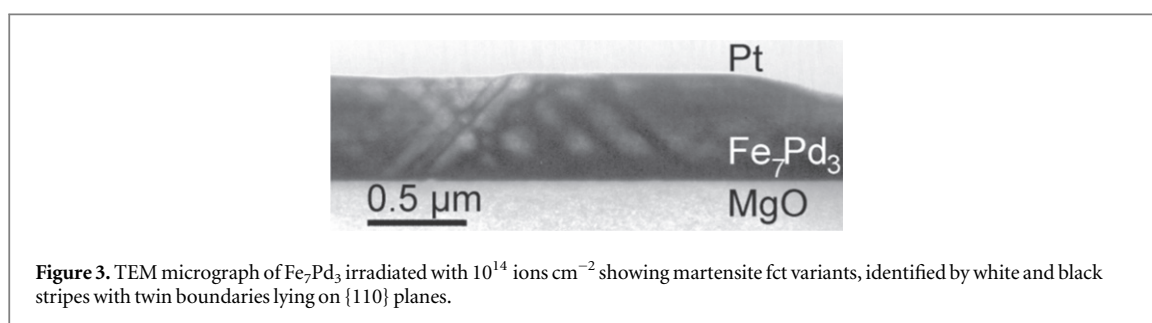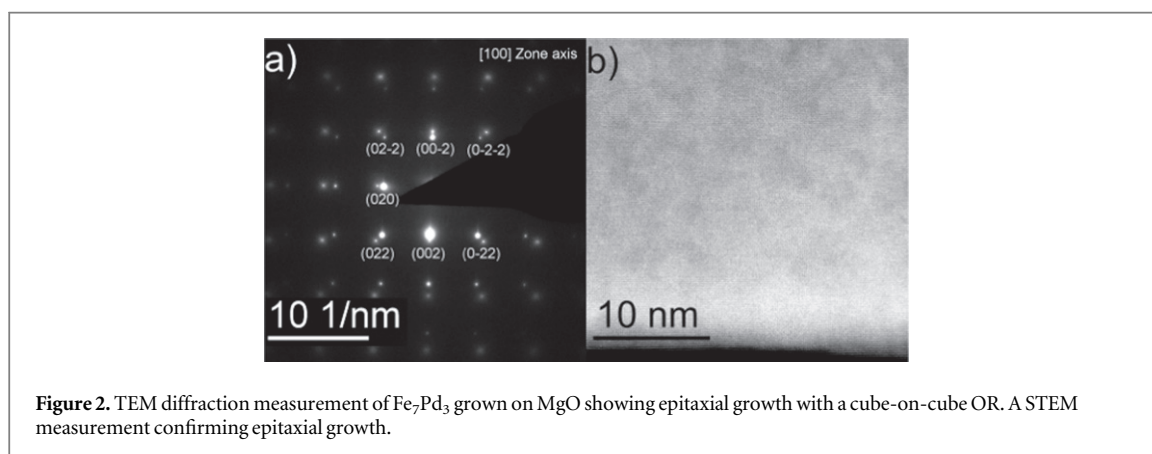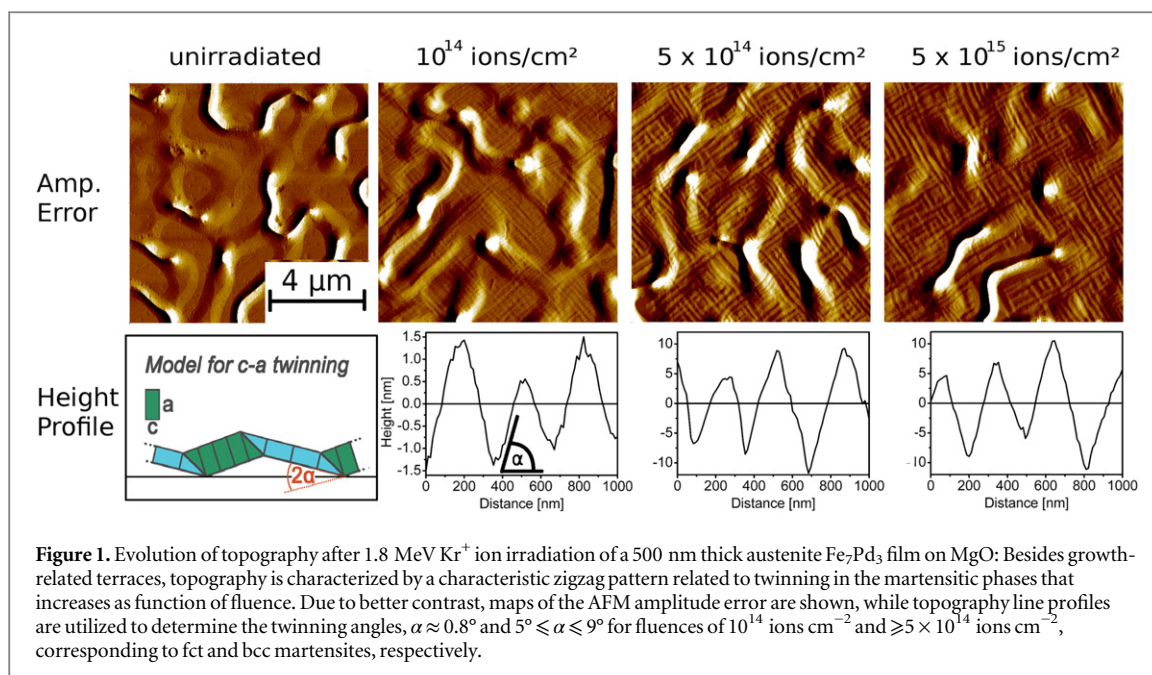## 3. Phenomenology of ion-irradiation-induced austenite ⇒ martensite transition

3.1. Modification of AFM topography by ion irradiation of austenite Fe$_7$Pd$_3$

Evidence in real space for ion-irradiation-induced austenite ⇒ martensite, followed by successive inter-martensite transitions, is most readily given by AFM surface topographs (figure 1).

While the topography of unirradiated austenite samples is dominated by terraces related to growth kinetics, ion irradiation results in formation-twinned martensite that is reflected on top of the surface by a characteristic zigzag profile. Assuming c-a twinning, a c/a ratio of around 0.97 (viz. degree of tetragonality) for the sample irradiated with 10^{14} ions cm^{-2} is directly determined via the relation $\alpha = 45° - \arctan(c/a)$, which is readily derived from the 'model for c-a twinning' sketched in figure 1 [24]. This value of 0.97 is close to 1 and indicates a slight tetragonal distortion and thus the fct phase. For higher fluences of $\geqslant 5 \times 10^{14}$ ions cm^{-2} twinning angles of $5° \leqslant \alpha \leqslant 9°$ indicate a strong tetragonal distortion and thus the bct/bcc phase. The c-a twinning model sketched in figure 1 is not applicable for the latter phases. Previous preliminary XRD studies revealed the bcc phase for a fluence of 5×10^{15} ions cm^{-2} [19]. This indicates that within the given accuracy, a phase transition at the surface occurs consistently throughout the bulk upon ion irradiating the austenite Fe$_7$Pd$_3$ film.

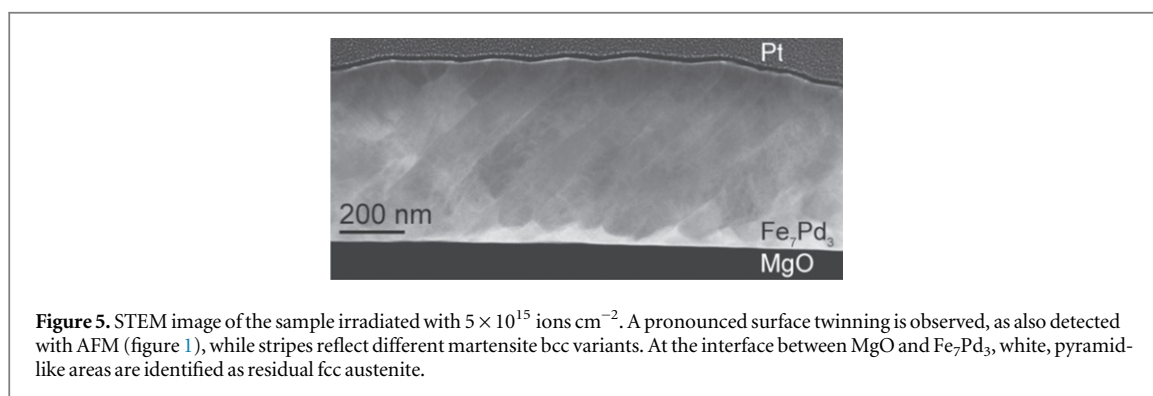### 3.2. Characterization of bulk nanostructure by HR-TEM

Although the AFM and XRD assessments are already conclusive regarding the basic phenomenon of ion-irradiation-induced austenite ⇒ martensite transition in Fe$_7$Pd$_3$, clearly more nanostructural characterization, particularly of the martensite domain (or, 'variant') network and defect state of the specimens, is desirable. HR-TEM is well suited for this purpose. Figure 2(a) shows the starting point of our study, viz. a SAED image in a [100] zone axis of MgO for the unirradiated sample. Diffraction spots of MgO and Fe$_7$Pd$_3$ are identified, yielding —as reference—a lattice parameter of MgO of (4.19 ± 0.06) Å, obtained by averaging the lattice parameters of three different lattice spacings (020), (002), and (022). The Fe$_7$Pd$_3$ out-of-plane and in-plane lattice parameters were determined to be (3.73 ± 0.06) Å and (3.77 ± 0.06) Å, respectively. In figure 2(b) a corresponding STEM measurement verifies cubic, epitaxial growth of Fe$_7$Pd$_3$ on MgO. Figure 3 shows a TEM micrograph of the

Figure 1. Evolution of topography after 1.8 MeV Kr$^+$ ion irradiation of a 500 nm thick austenite Fe$_7$Pd$_3$ film on MgO: Besides growth-related terraces, topography is characterized by a characteristic zigzag pattern related to twinning in the martensitic phases that increases as function of fluence. Due to better contrast, maps of the AFM amplitude error are shown, while topography line profiles are utilized to determine the twinning angles, $\alpha \approx 0.8°$ and $5° \leqslant \alpha \leqslant 9°$ for fluences of 10^{14} ions cm^{-2} and $\geqslant 5 \times 10^{14}$ ions cm^{-2}, corresponding to fct and bcc martensites, respectively.

Figure 2. TEM diffraction measurement of Fe$_7$Pd$_3$ grown on MgO showing epitaxial growth with a cube-on-cube OR. A STEM measurement confirming epitaxial growth.

Figure 3. TEM micrograph of Fe$_7$Pd$_3$ irradiated with 10^{14} ions cm^{-2} showing martensite fct variants, identified by white and black stripes with twin boundaries lying on {110} planes.

sample irradiated with 10^{14} ions cm^{-2}. Black and white stripes indicate different fct martensite variants with {110} twin boundaries.

A STEM image of the sample irradiated with 10^{14} ions cm^{-2} is depicted in figure 4. Employing Fast Fourier transformation (FFT), we have identified two differently aligned martensite variants. The lattice parameters are determined to be 3.80 Å and 3.79 Å for the short fct axis and 4.01 Å and 3.98 Å for the long fct axis, with an error of ±1.5%. These values result in an unusual high volume of the fct unit cell compared to the fcc phase and might be caused by TEM lamella preparation. The variants are related by a rotation of 90°, as expected for c-a twinning. At the interface, the fct unit cell is not rotated, indicating a gradual rotational transition from variant 1 to variant 2. This is in contrast to the sharp transition given in the schematic sketch in figure 1.

Figure 5 shows an STEM image of a sample irradiated with 5×10^{15} ions cm^{-2} that has been identified to reside in the bcc structure by AFM and XRD assessment. The characteristic stripes reflect different bcc

Figure 4. A STEM image of two fct martensite variants connected by a twin boundary. FFT reveals the lattice parameters and the orientation relation between the two variants. The unit cell of variant V1 is rotated slightly when approaching the V1–V2 interface. The short axis is rotated by approximately 90°.

Figure 5. STEM image of the sample irradiated with 5×10^{15} ions cm^{-2}. A pronounced surface twinning is observed, as also detected with AFM (figure 1), while stripes reflect different martensite bcc variants. At the interface between MgO and Fe$_7$Pd$_3$, white, pyramid-like areas are identified as residual fcc austenite.

martensite variants. At the interface between MgO and Fe$_7$Pd$_3$ white, triangle-shaped areas are identified as residual fcc austenite that are prevented from transformation due to substrate constraints. In the following, we focus again on the features of central interest, viz. a detailed investigation of the martensite stripes using FFT, as shown in figure 6. Dark and light stripes reflect differently aligned bcc martensite variants with [111] and [110] zone axis.

3.3. Modification of magnetic properties

As modifications of phases and structural properties in MSM alloys lead to changes in magnetic properties, we assess the nano- and macromagnetic properties during ion-irradiation-induced austenite ⇒ martensite transformation. For global characterization, SQUID magnetization measurements were performed; they are summarized in figure 7. For in-plane and out-of-plane characterization of each sample, the external magnetic field was aligned parallel to MgO$_{[100]}$ and along the MgO$_{[001]}$ directions (sample normal), respectively. For each measurement, the external magnetic field was swept between −80 kOe and 80 kOe. The diamagnetic contribution of the 0.5 mm thick MgO substrate was subtracted from all M(H) curves; it was determined by a linear fit to those parts of the uncorrected M(H) curves, where the magnetization started to decrease instead of showing saturation. The saturation magnetization of the unirradiated sample was (1016–1045) emu cm^{-3}, with successive increases along the transformation path. While the fct phase reveals a saturation magnetization of (1237–1290) emu cm^{-3}, the largest was the bcc phase with (1354–1386) emu cm^{-3}. These measurements are in accordance with previous measurements of (1080 ± 10) erg cm^{-3} for the fcc phase and 1220 erg cm^{-13} for the fct phase [32]. To explain the changes in magnetic hysteresis, two important effects introduced by ion irradiation must be considered: (1) Ion irradiation creates point defects, which interact with magnetic domain walls. (2) The crystal structure is changed from cubic (fcc, unirradiated) to tetragonal (fct, 10^{14} ions cm^{-3}) to cubic (bcc, 5×10^{15} ions cm^{-3}). Each crystal structure has its own magnetocrystalline anisotropy characteristics. Coercivity and remanence are extracted from the hysteresis loop and summarized together with the saturation magnetizations in table 2.
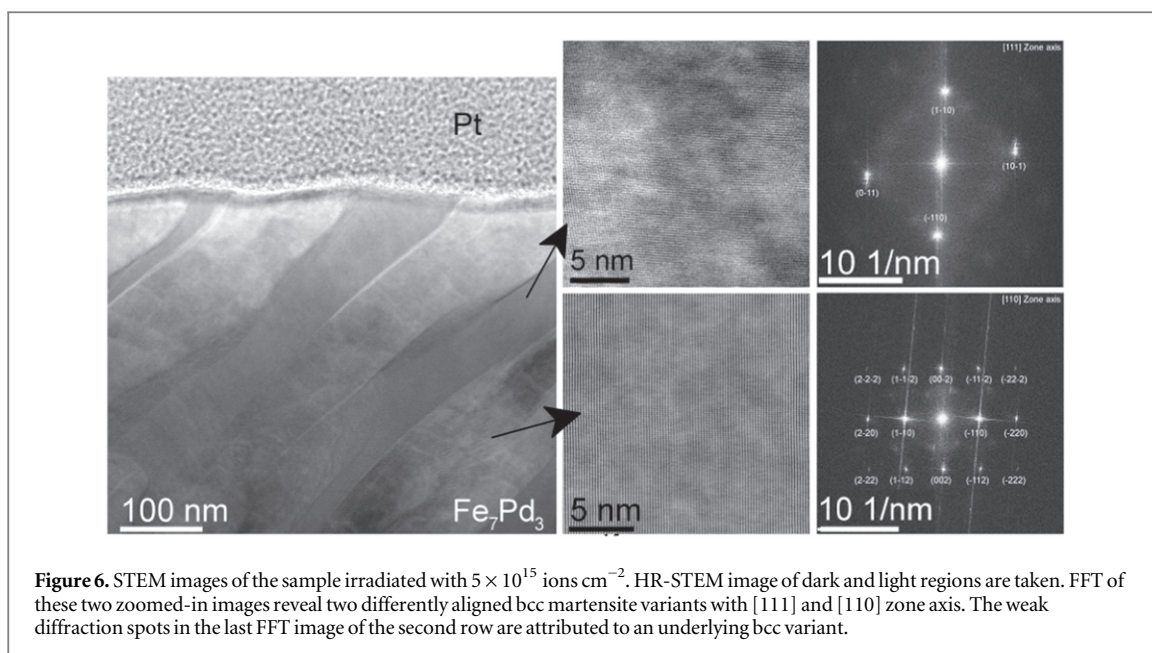
Figure 6. STEM images of the sample irradiated with 5×10^{15} ions cm^{-2}. HR-STEM image of dark and light regions are taken. FFT of these two zoomed-in images reveal two differently aligned bcc martensite variants with [111] and [110] zone axis. The weak diffraction spots in the last FFT image of the second row are attributed to an underlying bcc variant.
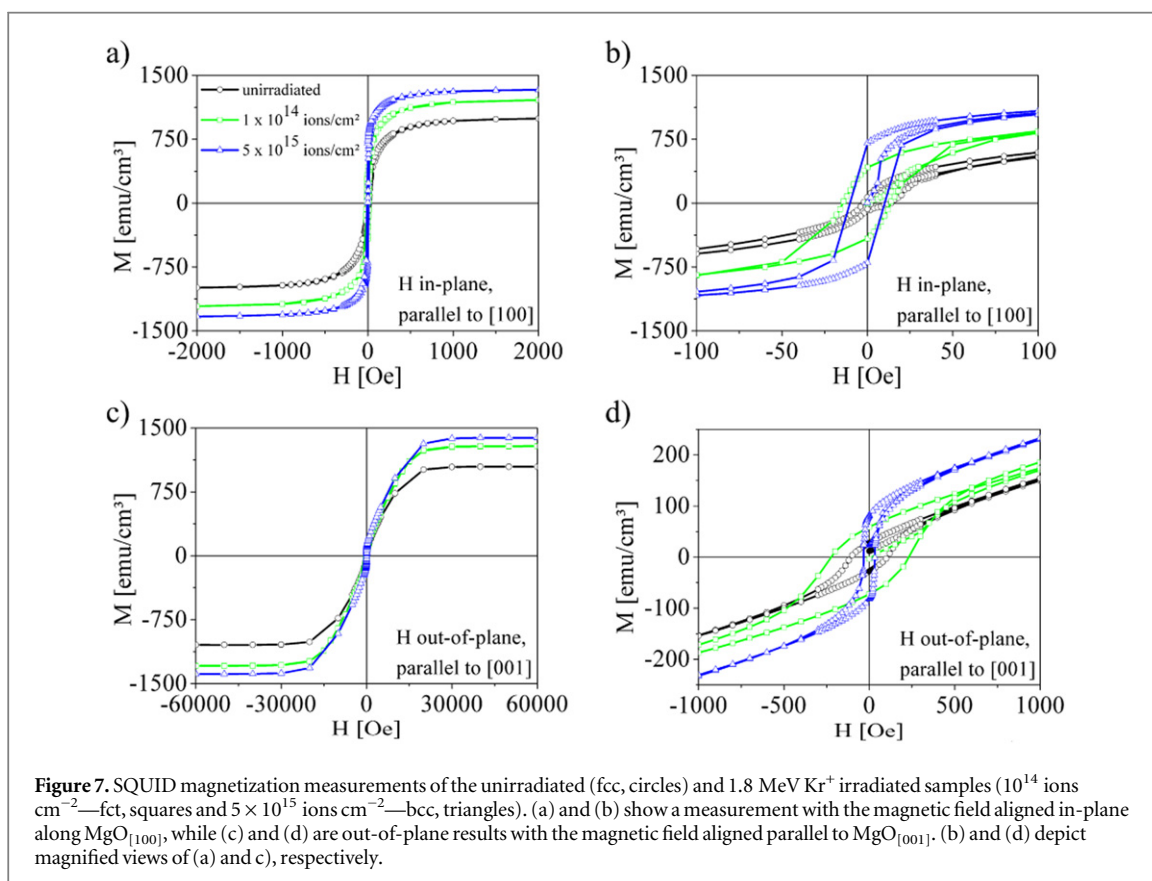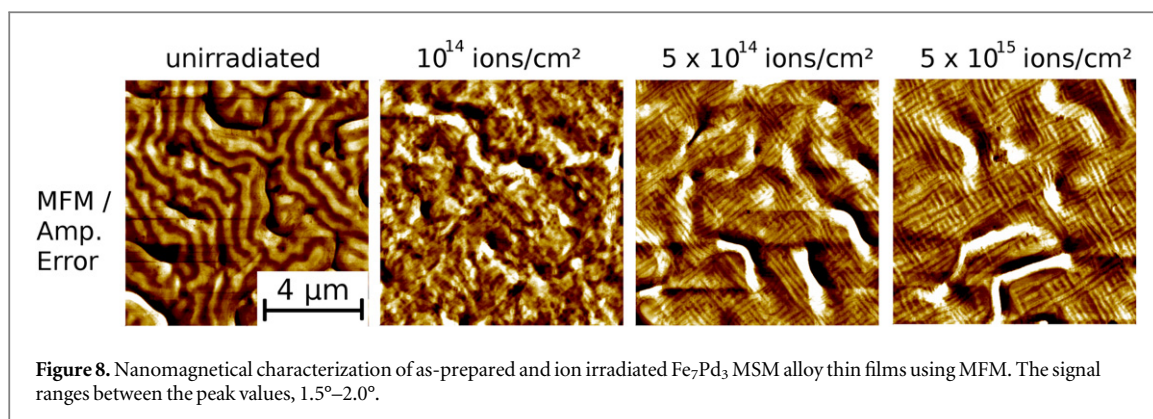

Figure 7. SQUID magnetization measurements of the unirradiated (fcc, circles) and 1.8 MeV Kr$^+$ irradiated samples (10^{14} ions cm^{-2}—fct, squares and 5×10^{15} ions cm^{-2}—bcc, triangles). (a) and (b) show a measurement with the magnetic field aligned in-plane along MgO$_{[100]}$, while (c) and (d) are out-of-plane results with the magnetic field aligned parallel to MgO$_{[001]}$. (b) and (d) depict magnified views of (a) and c), respectively.

Table 2. Saturation magnetization, coercivity, and remanence as function of ion fluence.

Phase, fluence	Saturation magnetiza-tion [emu cm^{-3}]	Coercivity, in-plane [Oe]	Coercivity, out-of-plane [Oe]	Remanence In-plane [emu cm^{-3}]	Remanence Out-of-plane [emu cm^{-3}]
fcc, unirradiated	1016–1045	2	107–110	69–86	28
fct, 10^{14} ions cm^{-2}	1237–1290	14	224–232	419–416	59–73
bcc, 5×10^{15} ions cm^{-2}	1354–1386	10	32–33	698–704	82

Figure 8. Nanomagnetical characterization of as-prepared and ion irradiated Fe_7Pd_3 MSM alloy thin films using MFM. The signal ranges between the peak values, 1.5°–2.0°.

Clearly, remanence in both magnetization directions, out-of-plane and in-plane, increases with fluence. Comparing the unirradiated sample with the one irradiated to 5×10^{15} ions cm^{-2}, we observe that the in-plane remanence increased by a factor of nine from (69–86) emu cm^{-3} to (698–704) emu cm^{-3}, while the out-of-plane remanence grew by a factor of three from 28 emu cm^{-3} to 82 emu cm^{-3}. The increase in remanence can be understood by an increasingly hindered movement of the magnetic domain walls due the interaction with defects. In contrast, there seems to be no direct correlation between coercivity and ion fluence. The in-plane coercivity for the irradiated and unirradiated samples varies between (2–14) Oe and can be neglected, while the unirradiated sample reveals (107–110) Oe. Irradiation with 10^{14} ions cm^{-2} nearly doubles coercivity to (224–232) Oe, while with fluence increasing to 5×10^{15} ions cm^{-2}, it decreases to a minimum of (32–33) Oe. From these observations it seem reasonable to assume that coercivity is mainly influenced by the magnetocrystalline anisotropy, and that point defects only play a minor role. In fact, austenite is established to reveal nearly isotropic magnetization behavior with a slightly preferred [111] axis [32], just as bcc martensite. The tetragonal structure of fct martensite, on the other hand, has a high tetragonal anisotropy constant $K_1 = 1.5 \times 10^5$ erg cm^{-3} [33] and the highest magnetocrystalline anisotropy of all phases—in direct correlation with magnetic anisotropy.

As for nanomagnetical characterization with MFM, all specimens were measured *as-prepared* or *as-irradiated*, i.e., prior to SQUID magnetization measurements; the results are summarized in figure 8. The unirradiated sample shows a well-defined and ordered MFM pattern consisting of alternating dark and bright stripes with a width in the range of 300 nm. This finding, which we have reported previously [34], indicates significant out-of-plane contributions to the magnetization, which, at first glance, is at odds with the cubic symmetry of the single crystalline austenite Fe_7Pd_3 film, as *in-plane* alignment of the magnetic moments is expected to reduce stray fields. As we demonstrated previously [34], however, a strong anisotropy caused by film stresses can explain this scenario, even quantitatively. Upon transformation to martensite, the two longer axes of the tetragonal unit cell constitute the easy axes of magnetization [32]. Since at least one of these axes must always be aligned *in-plane*, preferential *in-plane* orientation of the magnetization is expected in absence of stress-induced anisotropies. As a successive decrease of *out-of-plane* contributions to the magnetization with increasing fluence is, in fact, observed in the MFM measurements (figure 8), this finding indicates reduction of film stresses in the course of ion-irradiation-induced formation of martensite. In fact, stress reduction upon temperature-induced austenite ⇒ martensite transformations is a well-established phenomenon in 'classical' shape memory alloys, which stems from the adaptive nature of martensites, viz. accommodation of variants for stress reduction [35]. Even though stress reduction is observed due to the transformation process, the transformation itself is induced by an increase of stress due to ion irradiation, as explained in detail in section 4.

3.4. Reversible austenite ⇔ martensite phase transformation due to defect annealing

To study the reversibility of the ion-irradiation-induced austenite ⇔ martensite transformation, one sample was irradiated with 1.8 MeV 10^{15} ions cm^{-2} and subsequently annealed at 423 K for 1.5 h, 573 K for 1.5 h, and 723 K for 1 h. θ–2θ scans of the unirradiated, irradiated, and annealed samples are shown in figure 9. Ion irradiation leads to broadening of the peak that occurs as a result of a reduced coherence length in course of a proceeding fcc to fct phase transformation [12]. The FWHM doubles from 0.30° to 0.58°, while the intensity of the fcc peak at 48.3° falls to 18% of its initial value. Annealing leads to a partial recovery of the initial peak: the FWHM decreases and the intensity reaches 61% of its initial value. The FWHM and normalized intensities are summarized in table 3.
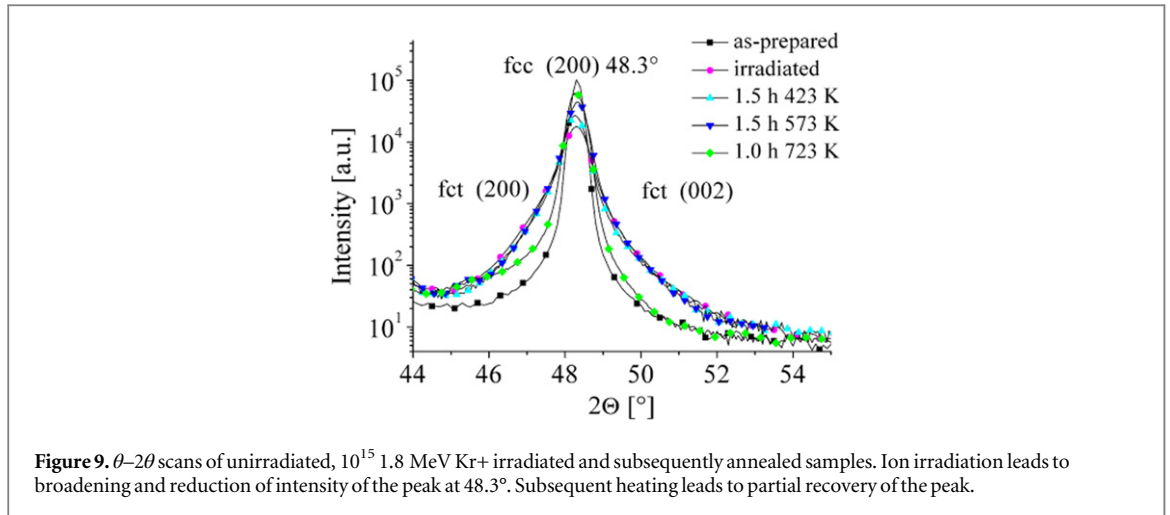
Figure 9. θ–2θ scans of unirradiated, 10^{15} 1.8 MeV Kr+ irradiated and subsequently annealed samples. Ion irradiation leads to broadening and reduction of intensity of the peak at 48.3°. Subsequent heating leads to partial recovery of the peak.

Table 3. The degree of fct martensite phase transformation is given by the intensity and the FWHM of the austenite fcc reflection. Ion irradiation with 1.8 MeV Kr$^+$ ions shows a fcc $\Leftrightarrow$ fct phase transformation, reflected by a decrease of the fcc intensity to 18% of its initial value and doubling of the FWHM. Annealing recovers the shape of the initial fcc reflection partly, thus reversing the transformation.

Condition	2θ [°]	FWHM [°]	Normalized Intensity [a.u.]
As-prepared	48.3	0.30	1.00
irradiated	48.3	0.58	0.18
1.5 h 423 K	48.3	0.49	0.26
1.5 h 573 K	48.3	0.47	0.44
1.0 h 723 K	48.3	0.42	0.61

4. Physical principles behind ion-irradiation-induced martensite transitions in Fe$_7$Pd$_3$

Despite discussing in-depth the phenomenology of ion-irradiation-induced multi-martensite transitions and related manifestations in materials properties, we have not yet clarified the underlying physical mechanism. Clearly, this mechanism will—as mentioned in section 1—involve short-range order within the system and/or mechanical stresses, which are both expected to be severely affected by ions.

4.1. Impact of ion irradiation on order

As for modifications of short-range order, the first route for ion irradiation to affect the austenite $\Leftrightarrow$ martensite and inter-martensitic transitions, Martin's 'driven alloy' concept [36] provides a comprehensive theoretical framework for in-depth understanding. Within the present scope, however, it suffices to contemplate a few qualitative essentials: we start by emphasizing that the Fe$_7$Pd$_3$ system generally is prone to short-range ordering tendencies. In fact, preference for Fe–Pd coordination has already been experimentally detected in Fe$_7$Pd$_3$ splats by a CEMS study [37]. Additional rationale for this behavior is also given by the phase diagram, which shows ordered phases throughout at sufficiently moderate temperatures. Irradiating Fe$_7$Pd$_3$ samples with energetic ions will certainly modify this order: While it is intuitively clear that collision cascades will be accompanied by mixing ('ion beam mixing') and thus disordering, ion-irradiation-induced ordering tendencies also occur owing to increased mobility within the alloy from the creation of excess vacancies and interstitials [38].

The impact of changes in short-range order induced by ion irradiation on the austenite $\Leftrightarrow$ martensite phase transformation has been studied by CEMS. CEMS detects changes in short-range order by probing the local environment of ^{57}Fe nuclei. CEMS experiments were performed on the unirradiated sample and the three 1.8 MeV Kr$^+$ irradiated samples with 10^{14} ions cm^{-2}, 5×10^{14} ions cm^{-2}, and 5×10^{15} ions cm^{-1}. The four spectra are shown in figures 10(b)–(e).

All four spectra show a typical six line pattern expected for ^{57}Fe due to the interaction of the nuclear states with the magnetic hyperfine field B_{eff}. Three hyperfine parameters can be extracted from these spectra [39]. The center shift (δ, so-called isomer shift) is given by the centroid of the spectra and is sensitive to chemical changes. An electric field gradient (EFG) at the nucleus, if present, produces a quadrupole line shift. An EFG is present for
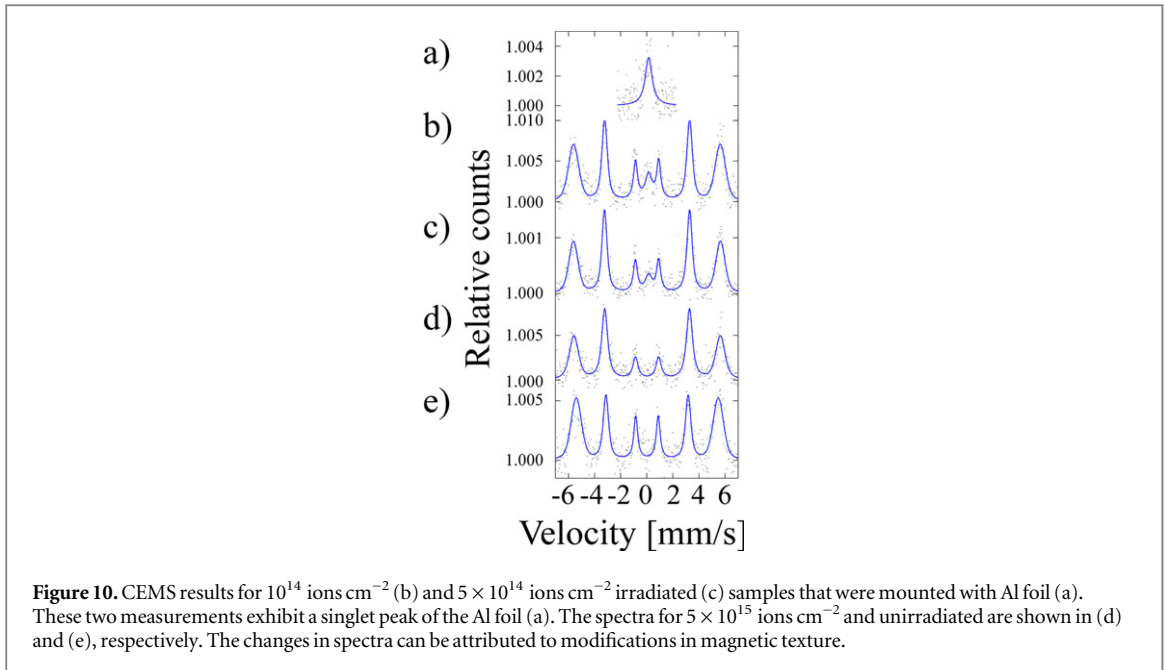
Figure 10. CEMS results for 10^{14} ions cm^{-2} (b) and 5×10^{14} ions cm^{-2} irradiated (c) samples that were mounted with Al foil (a). These two measurements exhibit a singlet peak of the Al foil (a). The spectra for 5×10^{15} ions cm^{-2} and unirradiated are shown in (d) and (e), respectively. The changes in spectra can be attributed to modifications in magnetic texture.

Table 4. Results from fitting the spectra (b)–(e) in figure 10. The center shift δ is given with respect to bcc Fe at room temperature. B_{eff}-max and the standard deviation $\sigma(B_{eff})$ are obtained by a Gaussian fit to $P(B_{eff})$.

Sample	δ [mm/s]	B_{eff} [T]	$\sigma(B_{eff})$ [T]	A23
Unirradiated	0.02(1)	33.1(1)	3.6(1)	1.8(1)
10^{14} ions cm^{-2}	0.02(1)	34.9(1)	3.6(1)	2.5(1)
5×10^{14} ions cm^{-2}	0.01(1)	34.9(1)	3.5(1)	2.9(1)
5×10^{15} ions cm^{-2}	0.02(1)	34.8(1)	3.5(1)	3.3(1)

noncubic materials as well as for disordered alloys. The magnetic hyperfine field (B_{eff}) present in magnetic materials can be extracted. In the present case, the broadened lines indicate a distribution $P(B_{eff})$ of B_{eff} due to a distribution of magnetic moments typical of disordered alloys. The Gaussian width $\sigma(B_{eff})$ of the distribution $P(B_{eff})$ is obtained from a fit. Table 4 shows the data obtained from fitting the four spectra.

For the first two samples, commercial Al foil was used inadvertently to secure the sample in the CEMS chamber. For this reason, there is a small single line at the center of the spectrum due to iron impurities. The Al foil alone yields the top spectrum in the plot (a), and the line width and center shift of this was used to fit these two sample spectra.

The maxima of the hyperfine magnetic field B_{eff}-max changes from 33.8 T for the unirradiated sample to (34.8—34.9) T for the irradiated samples. This change in B_{eff} is consistent with the change in magnetic texture leading to a small change in the demagnetization field. This is confirmed by the relative areas of the three lines on each side of the spectra given by: A3: A23: A1. A23 for the unirradiated sample is (1.8 ± 0.1) and it increases to (2.59 ± 0.1) for the 10^{14} ions cm^{-2}, (3.1 ± 0.1) for the 5×10^{14} ions cm^{-2}, and (3.5 ± 0.1) for the 5×10^{15} ions cm^{-2} irradiated sample. The relative intensities change from 3:1.8:1 to 3:3.5:1. A ratio of 3:0:1 describes a perpendicular orientation of the magnetic moments against the surface: a ratio of 3:4:1 describes an in-plane orientation. Thus, ion irradiation changes the magnetic texture from nearly random to nearly in-plane. The center shift (isomer shift δ), which is sensitive to chemical changes, does not show any changes. The Gaussian width of B_{eff}, $\sigma(B_{eff})$, remains constant for all four samples as 0.1 T. A quadrupole line shift (Δ) is expected for the fct phase due to an EFG, but was not observed. This shift is probably mixed into the linewidth.

4.2. Role of defect-induced stresses

Inserted point defects are expected to destabilize the austenite Fe$_7$Pd$_3$ crystal lattice in a twofold way. 1) Resulting global shear stresses acting on {110}[110] shear directions lead to lattice softening by increasing the martensite temperature due to the Clausius–Clapeyron equation [18, 40], while 2) the presence of interstitials is known to reduce elastic shear constants and result in lattice instability owing to their diaelasticity. While the latter can result in vitrification [41, 42] in systems prone to amorphization, it could potentially also lead to an austenite $\Rightarrow$ martensite transformation based on the notion that stress fields around point defects can largely be

accommodated by the adaptive nature of martensite (otherwise martensite would just be destabilized as much as austenite). This is exactly the point, where 1) and 2) merge again in the sense that 1) constitutes an effective homogenized, or global point of view, while 2) involves local stress fields around individualized defects.

Addressing this scenario more quantitatively, it is of note that the *as-grown* films reveal compressive stresses determined by the $\sin^2\psi$ method to be -0.29 GPa (employing Young's modulus E and Poisson ratio ν given in table 5) and reveal a typical martensite finish temperature of $M_f \approx 273$ K [43]. These stress levels can be understood based on a virtually stress-free growth of Fe_7P_3 on MgO at 1123 K and a larger thermal contraction of the MgO substrate during cooling, which results from the invar properties of Fe_7P_3 [23]. Ion irradiation is expected to increase these compressive stresses by generation of excess volume due to the production of Frenkel pairs in the course of collision cascades [44]. Within this scope, a central requirement for permanent ion-induced stresses is a sufficiently low defect mobility, which prevents their mutual annihilation or diffusion to the Fe_7Pd_3 surface or Fe_7Pd_3–MgO interface at room temperature. While vacancies in metals are usually characterized with a high enough migration enthalpy to prevent significant mobility at ambient conditions, interstitials are frequently characterized by very low migration enthalpies, some tens of meV. The assumption that the migration enthalpies for Fe interstitials (0.3 eV) and vacancies (0.55 eV) [45] are good estimates for Fe_7Pd_3 (for which no migration enthalpies are available), makes a Frenkel pair based defect mechanism perfectly plausible for the observed ion-irradiation-induced austenite $\Rightarrow$ martensite transformation. Strong corroboration for this interpretation is given by the annealing experiments in section 3.4, which reveal a reverse transformation back to austenite once the Frenkel pairs annihilate. These measurements thus provide an estimate of the interstitial migration enthalpy >723 K$\cdot k_B = 0.062$ eV (with Boltzmann constant k_B), i.e., high enough to prevent thermal Frenkel pair annihilation or migration to the interfaces at ambient conditions.

In accordance with recent molecular dynamics (MD) computer simulations on high-energy cascades in Fe [47] we assume that within a collision cascade first N^{def} defects are created, as predicted with good approximation by the binary collision approximation [31]. However, only a portion ξ of these defects survives [49]—partially due to spontaneous recombination, but predominantly due to annihilation within the subsequent thermal spike, as sketched in figure 11. In addition, the latter are also assumed to eliminate pre-existing defects from previous cascades within the thermal spike volume, as quantified by the number of atoms, N^{spike}, it contains. This allows us to write for the fraction, n, of Frenkel pairs relative to the total number of atoms:

$$\frac{dn}{d\Phi} = \frac{1}{\rho \cdot t}\left(\xi \cdot N^{def} - n \cdot N^{spike} \right) \tag{1}$$

where Φ, ρ and t denote the fluence, atomic density, and film thickness, respectively. By means of partial integration, this equation is readily solved for n, yielding:

$$n = \frac{\xi \cdot N^{def}}{N^{spike}}\left(1 - \exp\left(-\frac{N^{spike}}{\rho \cdot t}\Phi \right) \right) \tag{2}$$

Based on the Seitz and Koehler [46] treatment for a spherical thermal spike and the parameters given in table 5, we estimate $N^{spike} \approx 8 \cdot 10^6$. Assuming that the Frenkel pairs are inserted isotropically into the sample and employing the relative formation volume $\Delta V^f/\Omega_0$, the biaxial stress change due to irradiation-induced defects is estimated as:

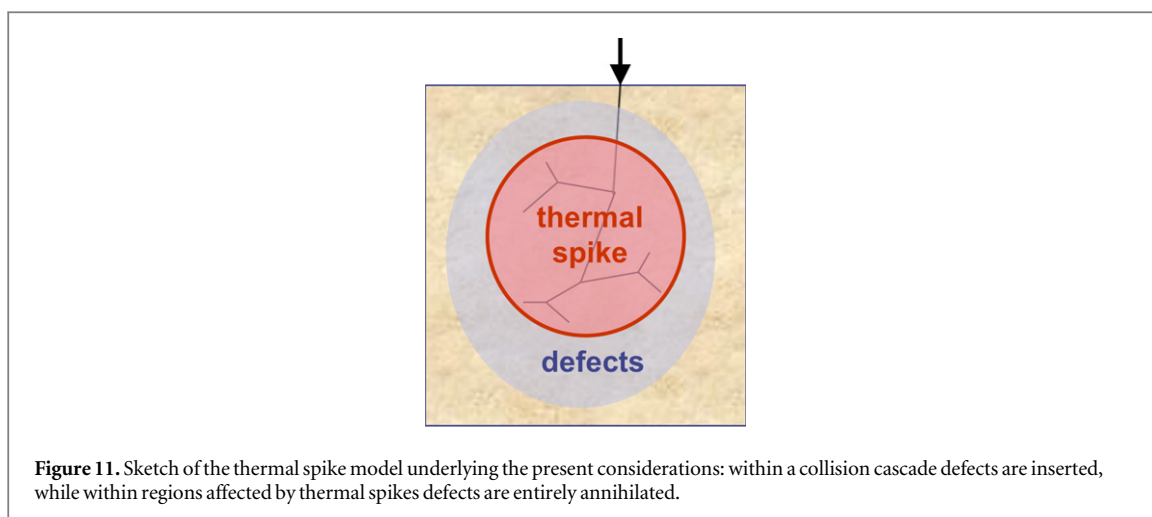$$\sigma = \frac{\Delta V^f}{3 \cdot \Omega_0} \cdot \frac{E}{(1 - \nu)} \cdot n. \tag{3}$$

As the present austenite $\Leftrightarrow$ martensite transformation constitutes a first-order phase transition, σ will shift the martensite temperature according to the Clausius–Clapeyron equation, as demonstrated for external stresses applied to bulk Fe–Pd crystals [49]:

$$\frac{dT}{d\Delta\sigma} = -2\frac{T \cdot \varepsilon}{\chi \cdot H} \approx -417\frac{K}{GPa} \tag{4}$$

where T, ε, χ, and H denote the martensite temperature, transformation strain, mass density, and latent heat, respectively, as given in [49]. Here the factor '2' accounts for biaxial stress (versus uniaxial in literature). Based on the typical martensite finish temperature, $M_f \approx 273$ K of films of this type [43], we can now estimate the fluence necessary to increase it, e.g., by 10 K using equation (2)–(4), and the parameters of table 5. According to equation (4) requiring a total stress change of 0.024 GPa, we obtain a required fluence of 1.7×10^{11} cm^{-2}, which constitutes a lower bound for the fluence necessary to induce fcc $\Rightarrow$ fct transformation, as annihilation at the surface and film–substrate interface has not been considered within these calculations. Furthermore, point defects are expected to act as obstacles that impede transformation in a twofold way. First, due to the long-range strain fields surrounding them, they are expected to pin twinning dislocations that mediate the austenite $\Rightarrow$

A Arabi-Hashemi *et al*

Table 5. Experimental parameters employed to model ion-irradiation-induced temperature shifts of martensite temperature: Ion energy Q, melting temperature T_x, specific heat c, mass density d, number of atoms within a thermal spike N^{spike}, number of created defects N^{def}, portion of stable defects ξ, formation volume of Frenkel pairs ΔV^f, atomic density ρ, Young's modulus E, Poisson ratio ν, and film thickness t. The parameters of Fe_7Pd_3 are estimated from the bcc Fe properties, where unavailable.

Q (eV)	T_x (K)	c (J kg-K^{-1})	d (kg m^{-3})	N^{spike} [46]	N^{def}	ξ [47, 48]	$\Delta V^f/\Omega_0$	ρ (Å^{-3})	E (GPa)	ν	t(Å)
$1.8 \cdot 10^6$	1673 [28]	450	891 [49]	$8 \cdot 10^6$	24 000 [31]	0.35	1.05 [50]	0.073 [21]	140 [51]	0.34 [20]	5000

Figure 11. Sketch of the thermal spike model underlying the present considerations: within a collision cascade defects are inserted, while within regions affected by thermal spikes defects are entirely annihilated.

martensite transformation. Second, in the course of their discrete nature, they will intrinsically introduce spatial heterogeneity of the austenite ⇒ martensite transition, with preferential formation of adaptive martensite around them, while other non-affected regions are expected to remain austenite. Both aspects can explain the higher fluences required for full transformation of the sample. In view of this analysis, the experimental observation of 'existence' of fct at a fluence of 10^{14} ions cm^{-2} is perfectly reasonable. Once the austenite ⇔ fct martensite transformation has occurred, a similar scenario will appear with the inter-martensite transformations (fct ⇔ bct; bct ⇔ bcc).

Additional effects occurring within thermal spikes, on the other hand, are expected to lower the threshold fluence for inducing austenite ⇒ martensite transformation. This can be rationalized by considering 1) the extremely high pressures that occur for some nanoseconds within thermal spikes following a Kr$^+$ impact. Upon cooling down, they are expected to trigger the transformation to martensite within the affected region, while the hystersis of the martensite ⇔ austenite transformation prevents the material from back-transformation to austenite. A very similar argument holds for 2) the shock waves that are generated in the course of a cascade. As we will demonstrate in a future work [52], we, in fact, have indications that shock waves are capable of affecting the austenite ⇔ martensite transformations. Two- and three-dimensional defects, such as voids or line defects including vacancy or interstitial loops, on the other hand are not generated in the course of ion irradiation: these defects would be easily observed within our STEM measurements.

5. Summary

In conclusion, our present work explores the capabilities of 1.8 MeV Kr$^+$ irradiation to tune phases and materials properties in single crystalline Fe$_7$Pd$_3$ MSM alloy thin films grown by molecular beam epitaxy on MgO substrates. Phenomenologically, a cascade of martensite transformations is observed with increasing fluence, starting with an fcc austenite to fct martensite transformation at 10^{14} ions cm^{-2} and followed by successive inter-martensite transformation to bct and bcc martensites at 5×10^{15} ions cm^{-2} and higher. This scenario can directly be tracked down by observing these structural transitions by XRD as well as following the development of a twin pattern in AFM surface reliefs and HR-TEM. The latter enabled us to characterize a twin boundary in fct martensite of Fe$_7$Pd$_3$ and unveiled the gradual nature of a c-a twin boundary. Local and global magnetic properties resulting from these phase transitions are additionally affected by ion-irradiation-induced defects. Most importantly, a vanishing stress-induced anisotropy after transformation to martensites, as indicated by MFM measurements, originates from stress relief. As for global magnetic properties, the saturation magnetization was measured to increase along the Bain transformation path, while the remanence and coercivity were found to scale with fluence, or defect density and magnetic anisotropy of the involved phases, respectively.

Furthermore, the ion irradiation, which induces the austenite ⇒ martensite transition, could be demonstrated to be—at least partially—reversible upon annealing. As for the physics behind these observations, two aspects are considered that both can result in phase transition shifts in Fe$_7$Pd$_3$, viz. ion-irradiation-induced changes in short-range order and stress state. CEMS measurements together with a quantitative stress model that takes into account the fluence dependent Frenkel pair formation spontaneous recombination unravels the central role of defect-induced film stresses. In a word, we have demonstrated that irradiation with energetic

heavy ions constitutes a very versatile approach to fine-tune the phase and physical properties in Fe_7Pd_3-based MSM alloys.

Acknowledgments

References

[1] Ullakko K, Huang J K, Kantner C, Handley R C O and Kokorin V V 1996 Large magnetic-field-induced strains in Ni_2MnGa single crystals *Appl. Phys. Lett.* **69** 1966–8
[2] James R D and Wuttig M 1998 Magnetostriction of martensite *Phil. Mag.* A **77** 1273–99
[3] Kussmann A and Jessen K J 1962 Invar-behavior and magnetic moments of gamma-phase of iron-palladium alloys *Phys. Soc. Japan* **17** 136
[4] Kußmann A and Jessen K 1963 *Magnetische und Dilatometrische Messungen zur Umwandlungskinetik der Eisen-Palladium-Legierungen Z. Metallkunde* **54** 504–10
[5] Gehanno V, Marty A, Gilles B and Samson Y 1997 Magnetic domains in epitaxial ordered FePd (001) thin films with perpendicular magnetic anisotropy *Phys. Rev.* B **55** 12552
[6] Sozinov A, Likhachev A A, Lanska N and Ullakko K 2002 Giant magnetic-field-induced strain in NiMnGa seven-layered martensitic phase *Appl. Phys. Lett.* **80** 1746–8
[7] Allenstein U, Ma Y, Arabi-Hashemi A, Zink M and Mayr S G 2013 Fe-Pd based ferromagnetic shape memory actuators for medical applications: biocompatibility, effect of surface roughness and protein coatings *Acta Biomater.* **9** 5845–53
[8] Ma Y, Zink M and Mayr S G 2010 Biocompatibility of single crystalline Fe70Pd30 ferromagnetic shape memory films *Appl. Phys. Lett.* **96** 213703
[9] Zink M, Szillat F, Allenstein U and Mayr S G 2013 Interaction of ferromagnetic shape memory alloys and RGD peptides for mechanical coupling to cells: from *ab initio* calculations to cell studies *Adv. Funct. Mater.* **23** 1383–91
[10] Bain E C and Dunkirk N Y 1924 The nature of martensite *Trans. Am. Inst. Min. Metall. Eng.* **70** 25–47
[11] Wechsler M S, Lieberman D S and Read T A 1953 *Trans. Am. Inst. Min. Metal. Eng.* **197** 1503
[12] Arabi-Hashemi A and Mayr S G 2012 Ion-irradiation-assisted phase selection in single crystalline Fe_7Pd_3 ferromagnetic shape memory alloy thin films: from fcc to bcc along the nishiyama-wassermann path *Phys. Rev. Lett.* **109** 195704
[13] Kakeshita T, Fukuda T and Takeuchi T 2006 Magneto-mechanical evaluation for twinning plane movement driven by magnetic field in ferromagnetic shape memory alloys *Mater. Sci. Eng.* **A438–440** 12–7
[14] Matsui M, Yamada H and Adachi K 1980 A new low temperature phase (fct) of Fe-Pd Invar *J. Phys. Soc. Japan* **48** 2161–2
[15] Oshima R, Kosuga K, Sugiyama M and Fujita F E 1981 Phase transition in Fe-Pd alloys *Sci. Rep. Res. Inst. Tohoku Univ.* **A29** 67–72
[16] Sugiyama M, Oshima R and Fujita F E 1984 Martensitic transformation in the Fe-Pd alloy system *Trans. Jpn. Inst. Met.* **25** 585–92
[17] Hamann S *et al* 2010 The ferromagnetic shape memory system Fe-Pd-Cu *Acta Mater.* **58** 5949–61
[18] Kato M and Pak H R 1984 Thermodynamics of stress-induced first-order phase transformations in solids *Phys. Stat. Sol.* **123** 415–24
[19] Mayr S G and Arabi-Hashemi A 2012 Structural defects in Fe-Pd-based ferromagnetic shape memory alloys: tuning transformation properties by ion irradiation and severe plastic deformation *New J. Phys.* **14** 103006
[20] Claussen I and Mayr S G 2011 Mechanical properties and twin boundary drag in Fe-Pd ferromagnetic shape memory foils—experiments and *ab initio* modelling *New J. Phys.* **13** 063034
[21] Mayr S G 2012 Energetic and thermodynamic aspects of structural transitions in Fe-Pd ferromagnetic shape memory thin films: an *ab initio* study *Phys. Rev.* B **85** 014105
[22] Gruner M E and Entel P 2011 Impact of local lattice distortions on the structural stability of Fe-Pd magnetic shape-memory alloys *Phys. Rev.* B **83** 214415
[23] Edler T, Hamann S, Ludwig A and Mayr S G 2011 Reversible fcc ⟨−⟩bcc transformation in freestanding epitaxially grown Fe-Pd ferromagnetic shape memory films *Scripta Mater.* **1** 89–92
[24] Ma Y, Setzer A, Gerlach J W, Frost F, Esquinazi P and Mayr S G 2012 Freestanding single crystalline Fe-Pd ferromagnetic shape memory membranes—role of mechanical and magnetic constraints across the martensite transition *Adv. Funct. Mater.* **22** 2529–34
[25] Edler T and Mayr S G 2010 Film lift-off from MgO: freestanding single crystalline Fe-Pd films suitable for magnetic shape memory actuation—and beyond *Adv. Mater.* **22** 4969–72
[26] Kühnemund L, Edler T, Kock I, Seibt M and Mayr S G 2009 Epitaxial growth and stress relaxation of vapor-deposited Fe-Pd magnetic shape memory alloy films *New J. Phys.* **11** 113054
[27] MgO substrates provided by Crystec GmbH, Berlin, Germany
[28] Massalski T B 1986 *Binary Alloy Phase Diagrams* vol 2 (Metals Park, OH: American Society for Metals)
[29] Edler T, Buschbeck J, Mickel C, Fähler S and Mayr S G 2008 Mechanisms of stress generation and relaxation during pulsed laser deposition of epitaxial Fe-Pd magnetic shape memory alloy films on MgO *New J. Phys.* **10** 063007
[30] Birkholz M 2006 *Thin film Analysis by X-Ray Scattering* (Weinheim, Germany: Wiley)
[31] Ziegler J F, Biersack J P and Littmark U 1985 *The stopping and range of ions in matter* vol 1 (New York: Pergamon)
[32] Cui J, Shield T W and James R D 2004 Phase transformation and magnetic anisotropy of an iron-palladium ferromagnetic shape-memory alloy *Acta Mater.* **52** 35–47

[33] Buschbeck J *et al* 2009 Full tunability of strain along the fcc-bcc Bain path in epitaxial films and consequences for magnetic properties *Phys. Rev. Lett.* **103** 216101

[34] Landgraf A, Jakob A M, Ma Y and Mayr S G 2013 Nanoscale magneto-structural coupling in as-deposited and freestanding single crystalline Fe7-Pd3 ferromagnetic shape memory alloy thin films *Sci. Technol. Adv. Mater.* **14** 045003

[35] Khachaturyan A G, Shapiro S M and Semenovskaya S 1991 Adaptive phase formation in martensitic transformation *Phys. Rev.* B **43** 10832–43

[36] Martin G and Bellon P 1996 *Driven alloys Solid State Phys.* **50** 189

[37] Claussen I, Brand R, Hahn H and Mayr S G 2012 Relaxation scenarios in Fe-Pd and Fe-Pd-Cu magnetic shape memory splats—short range order and microstructure *Scripta Mater.* **66** 163–6

[38] Riviere J P 1995 *Application of particle and laser beams in material technology* (Netherlands: Kluwer) pp 53–76

[39] Gütlich E A and Trautwein A 2011 *Mößbauer Spectroscopy and Transitional Metal Chemistry* (Berlin: Springer)

[40] Sugiyama M, Oshima R and Fujita F E 1986 Mechanism of FCC-FCT thermoelastic martensite transformation in Fe-Pd alloys *Trans. Jpn. Inst. Met.* **25** 719–30

[41] Nordlund K, Ashkenazy Y, Averback R S and Granato A V 2005 Strings and interstitials in liquids, glasses and crystals *Europhys. Lett.* **71** 625

[42] Granato A V 1992 Interstitialcy model for condensed matter states of face-centered-cubic metals *Phys. Rev. Lett.* **68** 974

[43] Ma Y and Mayr S G 2013 Nanoindentation response of substrate-attached and freestanding single-crystalline Fe$_7$Pd$_3$ ferromagnetic shape memory thin films around the martensite transition—impact of constraints and beyond *Acta Mater.* **61** 6756–64

[44] Mayr S G and Averback R S 2003 Effect of ion bombardment on stress in thin metal films *Phys. Rev.* B **68** 214105

[45] Ehrhart P 1991 *Landolt-Börnstein: Numerical data and Functional Relationships in Science and Technology* vol 3 (Heidelberg: Springer)

[46] Seitz F and Köhler J S 1956 Displacement of atoms during irradiation *Solid State Phys.* **2** 305–448

[47] Stoller R E 2012 *Comprehensive Nuclear Materials* vol 1 ed R J M Konigs (Amsterdam: Elsevier) p 293

[48] Zarkadoula E *et al* 2013 The nature of high-energy radiation damage in iron *J Phys. Condens Matter* **25** 125402

[49] Kato H, Liang Y and Taya M 2002 Stress-induced FCC/FCT phase transformation in Fe-Pd alloy *Scripta Mater.* 2002 **46** 471–5

[50] Ehrhart P 1983 *Dimensional Stability and Mechanical Behavior of Irradiated Metals and Alloys* vol 1 (London: British Nuclear Energy Society) p 101

[51] Muto S, Oshima R and Fujita F E 1990 Elastic softening and elastic strain energy consideration in the fcc-fct transformation of Fe-Pd alloys *Acta Metall. Mater.* **38** 685–94

[52] Bischoff A, Arabi-Hashemi A, Ehrhard M, Lorenz P, Zimmer K and Mayr S G 2015 unpublished results